Paper-based porous graphene/single-walled carbon nanotubes supported Pt nanoparticles as freestanding catalyst for electro-oxidation of methanol

Qiang Zhang[a,b], Fang Yue[a,b], Lijian Xu[a,b], Chenxue Yao[a,b], Rodney D. Priestley[c], Shifeng Hou[b,*]

[a] School of Chemistry and Chemical Engineering, Shandong University, 27 Shanda Nanlu, Jinan, 250100, PR China
[b] National Engineering Research Center for Colloidal Materials, Shandong University, Jinan, Shandong, 250100, PR China
[c] Department of Chemical and Biological Engineering, Princeton University, Princeton, NJ, 08544, United States

ARTICLE INFO

ABSTRACT

In this paper, we designed a facile strategy to prepare a freestanding 3D interconnected embossed graphene (e-RGO)-single wall carbon nanotubes (SWCNTs) paper supported Pt nanoparticles (Pt/e-RGO-SWCNT) without binder, which can be used as a flexible and robust electrode for methanol oxidation. The 3D porous e-RGO was prepared by using monodispersed polystyrene (PS) spheres as sacrificial templates to suppress the re-stacking of RGO sheets. Meanwhile, the SWCNTs penetrated through the e-RGO, and thus weaved them into a scalable film to provide an integrative conductive framework. Benefited from their high surface area, 3D porous inter-connected architecture, and good electrical conductivity, the Pt/e-RGO-SWCNT catalyst exhibited much higher electrocatalytic activity and durability for methanol oxidation than Pt/e-RGO and Pt/RGO catalysts. More importantly, the Pt/e-RGO-SWCNT is demonstrated to be outstanding flexible electrocatalysts, and the electrocatalytic performances under the different distorted situation (such as folded and rolled states) are almost the same as the normal state.

1. Introduction

The increasing advent of flexible electronic products, such as flexible cell phones, electronic paper and wearable devices, has arisen due to lightweight, portable, foldable (or twistable), wearability [1–4]. In this context, direct fuel cells (DFCs), with high energy density and low environmental impacts, are considered as potential power sources [5–11]. Developing foldable energy devices with robust mechanical property and high electrochemical activity has received growing interests. Recently, advancements in flexible energy storage system have resulted in next generation supercapacitors, rechargeable batteries and solar cells [12,13]. Such outstanding achievements have inspired the preparation of flexible fuel cells [14–16], in which highly active electro catalysts are loaded within a flexible support without use of any binder. The inactive and electrical insulating binders induce the reduction of the contact area between electrolytes and catalytic active sites, leading to the unsatisfactory catalytic activities [17,18]. Despite the demand, to our knowledge, there are no reports involving flexible electrodes for DFCs.

Most efforts focused on investigating suitable conductive substrates with flexibility as electrodes [19], such as conducting polymers [20], metals and metal nanoparticles/nanowires [21], carbon materials (carbon nanotubes [22], graphene paper (GP) [23], graphene foam [24], *etc.*). Among plenty of conductive supports, GP assembled by individual graphene sheet and graphene oxide has attracted significant attention as an excellent candidate for portable and flexible electrode materials. This is mainly attributed to their unique properties containing high surface area [25], excellent electrical conductivity [26], superior mechanical strength and flexibility [27]. Li et al. [28] reported uniformed graphene films formed on a membrane filter by a vacuum filtration strategy. However, the restacking or aggregation of RGO sheets severely reduces the specific surface area and results in limited performances [29]. To overcome this problem, Chen and co-workers [30] introduced Ni nanoparticles as "spacer" to suppress the restacking of graphene sheets and generate amounts of meso/macropores. Also, a direct laser reduction method was used to lowering the aggregation of RGO film, the resultant products of freestanding films displayed high electrical conductivity and high surface area [31]. In short, while these two synthetic routes can both prepare freestanding film with high conductivity and suppress the aggregation of GP, their relatively high cost and multi-step processes have limited their large-scale practical applications. What's more, Zhu et al. [32] reported a freestanding graphene/SWCNT hybrid membrane for MoS_x deposition, which was applied for hydrogen evolution reaction with remarkable catalytic

activity. The introduction of CNT favors in ion transport and can weave the electrode into a flexible film. Particularly, it is expected for the 3D hierarchical porous films consisting of 1D CNTs and 2D graphene to integrate the outstanding properties of these two components [33]. This gives an inspiration that porous graphene/SWCNT paper as support for distributing catalysts may show high electrochemical properties for methanol oxidation reaction (MOR).

Herein, we presented a scalable synthetic route to form a free-standing 3D interconnected porous e-RGO-SWCNT paper, in which PS spheres were used as a hard template, and SWCNTs were then assembled to insert through the film to facilitate the penetration of the electrolyte into the inner structure of the 3D porous electrode. The Pt/e-RGO-SWCNT exhibits excellent electrochemical performances towards MOR with a peak current density of 191.7 mA mg^{-1}, which is much higher than that on the comparative electrodes, *i.e.*, Pt/e-RGO (109.7 mA mg^{-1}) and Pt/RGO (68.5 mA mg^{-1}). This can be attributed to high surface area, 3D porous interconnected architecture and good electrical conductivity on Pt/e-RGO-SWCNT. Furthermore, the electro catalytic performances of Pt/e-RGO-SWCNT under different distorted situations (such as folded and rolled states) are almost the same as the normal state, which indicate that the as-obtained catalysts are flexible with good catalytic performances.

2. Experimental section

2.1. Materials and characterization

Chloroplatinic acid hexahydrate (H$_2$PtCl$_6$·6H$_2$O), sulphuric acid (H$_2$SO$_4$), methanol (CH$_3$OH), ammonium persulfate ((NH$_4$)$_2$S$_2$O$_8$, purity: ≥98%) and hydroiodic acid (HI, purity: ≥55%) were from Sinopharm Chemical Reagent Co., Ltd. Styrene (purity: ≥ 99%) and acrylic acid (purity: ≥99%) were obtained from Sigma-Aldrich Co., USA. The water solution of SWCNT dispersion (0.15 wt%) were obtained from Nanjing XFNANO Materials Tech., Co., Ltd. Ultrapure water (resistance: 18.25 MΩ cm^{-1}) was utilized as a solvent throughout the experiments. The quartz tube furnace (OTF-1200X) was purchased from Hefei Crystal Materials Technology Co., Ltd., China.

Scanning electron microscopy (SEM, SU8010, Hitachi, Japan), Transmission electron microscope (TEM, JEM-1011, Japanese Electronics Co. Ltd, Japan), and high-resolution TEM (HRTEM, Tecnai G2 F20, FEI, USA) were used to characterize the morphology and structure of the as-prepared materials. X-ray diffraction (XRD) measurements were conducted on a diffractometer (D8 Advance, Bruker Ltd, Germany) with Cu Kα radiation to determine the phase purity and crystal structure of the products. Elemental-mapping analysis were measured by EDS equipped on a Hitachi SU8010 SEM. X-ray photo-electron spectroscopy (XPS) analysis of samples was carried out on a photoelectron spectrometer (Thermo ESCALAB 250 X-ray) using a monochromatic Al Kα X-ray source. The specific surface area and corresponding pore size distribution curves of the films were measured from the Brunauer-Emmett-Teller (BET) and Barrett-Joyner-Halenda (BJH) analysis of desorption data using the Micromeriics ASAP 2020 instrument.

2.2. Preparations of electrocatalysts

2.2.1. Synthesis of PS latex suspension

Mono-dispersed PS latexes were synthesized by surfactant-free emulsion polymerization (SFEP) in a three-necked flask, as illustrated in previous reported procedures with slight modification [34,35]. Typically, 10 mL of styrene and 1.5 mL of acrylic acid were added into ultrapure water (150 mL) under stirring in a three-necked flask, and then the mixture was degassed with N$_2$ for 1 h followed by heating to 80 °C. Afterwards, ammonium persulfate (APS, 0.07*g*) was dissolved into ultrapure water (7 mL), and then was slowly added into the flask. The mixture was then polymerized while refluxing for 4 h. Finally, the

resulting PS spheres were centrifuged and washed several times with water to obtain a water-suspended products for further measurements. PS spheres with different size were prepared by tuning the concentration of the precursors. The sizes of spheres increased with the increasing the monomer concentration. The diameter of the PS spheres with 200 nm, 600 nm and 3 μm were obtained. The resulting samples were denoted as PS-0.2, PS-0.6 and PS-3, respectively.

2.2.2. Synthesis of e-RGO-SWCNT films

In a synthetic procedure, 7 mL of GO dispersion (10 mg ml^{-1}) prepared by modified Hummers' method [36], which was dispersed into 28 ml ultrapure water under sonication. PS-0.6 (1.4 mL) was added dropwise into the GO suspension, followed by sonication for 20 min to obtain a brown-grey coagulation (2:1 wt ratio of GO/PS). Subsequently, the SWCNTs (3.34 mL, 0.15 wt%) mixed with the above solution were sonicated for 40 min and stirred for 10 min. Subsequently, the obtained brownish black suspension was poured onto an organic membrane (diameter: 9 cm, pore size: 0.22 μm) by vacuum filtration. The corresponding paper-like film was prepared after drying in air, and then peeled from the filtration membrane. For enhancing the flexibility, the freestanding film was immersed into an HI solution (45 wt%) at 90 °C for 4 h by an oil bath [37]. The resulting film was washed with ethanol three times and then dried at 60 °C for overnight. Finally, the film was calcined to 500 °C under Ar atmosphere (100 sccm) for 1 h, with a heating speed of 5 °C min^{-1} in a tube furnace. The resultant samples were assigned as e-RGO-SWCNT (0.2), e-RGO-SWCNT (0.6) and e-RGO-SWCNT (3), corresponding to different size of PS with diameters of 200 nm, 600 nm and 3 μm, respectively. For comparison, e-RGO films were also prepared similarly without the SWCNTs and the RGO films were fabricated using only GO suspension as the precursor with the similar procedure.
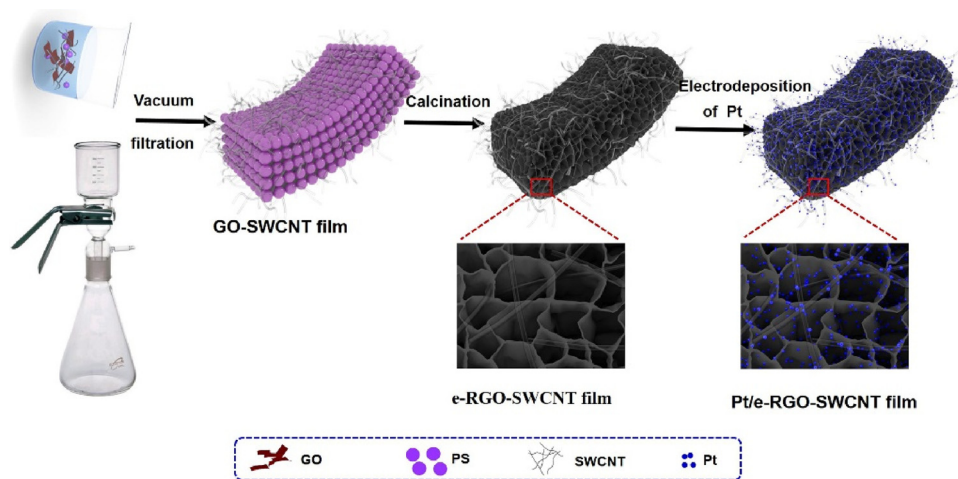
2.2.3. Synthesis of Pt/e-RGO-SWCNT films

The electrodeposition of Pt nanoparticles on e-RGO-SWCNT was carried out in 3.0 mM H$_2$PtCl$_6$ + 0.5 M H$_2$SO$_4$ with the potential of −0.2 V, according to previous literature [38]. Given that current efficiency is 100%, the Pt loading mass on the films was calculated *via* the charge integrated according to Faraday's law [39]. The charge for the deposition of Pt was 0.05 C, which is corresponded to the Pt loading of 0.025 mg and labeled as Pt/e-RGO-SWCNT. For comparison, the different charges were also deposited, such as 0.01, 0.03 and 0.1 C. Meanwhile, Pt particles on the Pt/e-RGO and Pt/RGO were also prepared with the same of depositing charge of 0.05 C.

2.3. Electrochemical test

All electrochemical experiments (cyclic voltammetric (CV), chronoamperometric (CA) and electrochemical impedance spectroscopy (EIS)) were conducted in a conventional three-electrode cell with CHI 760E electrochemical analyzer (Shanghai CH Instrumental *Co.*). A platinum wire and a KCl-saturated calomel electrode (SCE) electrode were used as the anxiliary electrode and reference electrode, respectively. The freestanding and flexible Pt/e-RGO-SWCNT hybrid membrane was employed as the working electrode with an effective working area controlled to about 1 cm × 0.5 cm.

For comparison, Pt/e-RGO and Pt/RGO films as working electrodes were also fabricated by the same method. In order to evaluate the catalytic activity and stability of as-prepared samples, the cyclic voltammetry (CV) curves were measured between −0.2 V–1.0 V (*vs*. SCE) and the chronoamperometry (CA) analysis were performed at 0.6 V in N$_2$-staturated 0.5 M H$_2$SO$_4$ + 1.0 M CH$_3$OH solution with a scan rate of 50 mV/s. Electrochemical impedance spectroscopy (EIS) was conducted in the solution of 5.0 mM K$_3$[Fe(CN)$_6$]/K$_4$[Fe(CN)$_6$] (1:1) with frequencies ranging between 0.1 and 100 kHz at the potential of 0.2 V.

Scheme 1. Schematic illustration for the Pt/e-RGO-SWCNT film.

3. Results and discussion

### 3.1. Physical characterization

The schematic illustration of Pt/e-RGO-SWCNT film is presented in Scheme 1 , and the corresponding details of the synthesis protocols are described in the experimental section. The digital image shows that the e-RGO-SWCNT (0.6) is a macroscopic film, and the lateral size reaches about 6 cm (Fig. 1a). The size of the membrane is controlled by the diameter of the filtration film. The films possess outstanding free-standing properties and high flexibility (see inset in Fig. 1a). The as-prepared PS spheres are monodisperse with an average diameter of 600 nm, which can serve as sacrificial templates to prevent the aggregation of RGO sheets (Fig. S1a). A SEM image (see Fig. 1b) reveals that the e-RGO-SWCNT (0.6) with crumpled and rough textures is wrapped with the framework of PS. The e-RGO-SWCNT (0.6) film exhibits a thickness of approximately 15 μm according to the SEM images of the side view (see Fig. 1c). The overall thickness of the membrane can be easily regulated by tuning the mass of the precursors. Upon high-magnified cross sectional SEM image (see Fig.1d), the e-RGO-SWCNT (0.6) can be prepared with the similar pore size as the PS template of 600 nm. The interlaced SWCNTs penetrate through e-RGO and thus weave them into a stable film. The SWCNTs offer an integrative conductive 3D structures, which has the benefit for the ionic and electronic transport throughout the film [40]. Furthermore, the introduction of SWCNTs can also prevent the RGO from aggregating and provide a large surface area, thereby remarkably enhancing the electro-catalytic performance. The TEM and HRTEM images (see Fig. 1e and f) further clearly demonstrate the assembled 3D porous interconnected architecture by removing the PS templates after calcination.

Fig. 2a, b shows SEM images of the cross-section of Pt/e-RGO-SWCNT (0.6) film. It can be seen that Pt nanoparticles are threaded across the film along the SWCNTs, which is different from the previous report with the Pt and Pd nanoparticles only depositing on the outer surface of the substrate [41]. The similar morphologies of the Pt/e-RGO-SWCNT (0.2) and Pt/e-RGO-SWCNT (3) are also observed as illustrated in Figs. S2b and d and S3c, respectively. The SWCNT networks facilitate the delivery of the electrolyte into the inside of the 3D porous frame, thus favoring the Pt nanoparticles throughout the whole e-RGO-SWCNT matrix rather than distribute on the outmost surface only. Pt nanoparticles with an average size of about 100 nm are grown atop the e-RGO-SWCNT (0.6) film by the potentiostatic reduction method (Fig. S4a). Elemental mapping of Pt/e-RGO-SWCNT confirms that Pt, C and O are homogeneously distributed in the 3D porous interconnected structure (Fig. S4b). Typical TEM images of Pt/e-RGO-SWCNT (0.6) and Pt/e-RGO-SWCNT (0.2) are provided in Figs. 2c and S2d, which clearly indicate that the Pt nanoparticles distribute homogeneously on the e-RGO-SWCNT. For comparison, e-RGO (0.6) and Pt/e-RGO (0.6) films were also prepared (see Fig. S5). Obviously, no particles are found across the internal porous framework from the cross section of the film.

The pore structures of the e-RGO and e-RGO-SWCNT films were explored by the nitrogen adsorption-desorption isotherm measurements (see Fig. 3a). The nitrogen adsorption-desorption isotherm of e-RGO and e-RGO-SWCNT reveals a type-IV isotherm, indicating the pores on the samples are dominantly mesopores. The hysteresis loop of the e-RGO-SWCNT expended almost $P/P_0 = 1$, indicating complete filling of the mesopores [42]. The pore size distribution of e-RGO (see the inset in Fig. 3a) obtained by the Barrett-Joyner-Halenda (BJH) model reveals the average pore size of around 3 nm. After the embedding of SWCNT, the e-RGO-SWCNT shows a typical bimodal pore size system. Besides the similar mesopores with the size centered at 3 nm, e-RGO-SWCNT also exhibits small mesopores with size centered at 11 nm. Therefore, it can be demonstrated that the pore structure of the PS template was well preserved after calcination. The result exhibits that the e-RGO-SWCNT has larger Brunauer-Emmett-Teller (BET) surface areas of 93.84 $m^2\,g^{-1}$ than that of RGO (5.45 $m^2\,g^{-1}$) and e-RGO (29.52 $m^2\,g^{-1}$). The results indicate that the PS and SWCNT prevents RGO from agglomeration, and thus lead to higher surface area in comparison with RGO. The pore size distribution of e-RGO (see the inset in Fig. 3a) obtained by the Barrett-Joyner-Halenda (BJH) model reveals the average pore size of around 3 nm. After the embedding of SWCNT, the mesopores is approximately 11 nm. The interlaced SWCNTs threaded between e-RGO can increase the electrode/electrolyte contact area and supply abundant diffusion channels for electrolyte infiltration [40]. The crystal features of the as-synthesized composite films were investigated by XRD technique. In Fig. 3b, RGO, e-RGO, e-RGO-SWCNT exhibit similar XRD patterns with a diffraction peak at $2\theta = 25.5°$, assigned to the typical graphitic C (002) [43]. For Pt/e-RGO-SWCNT, the four additional diffraction peaks at 2θ values about 40.0, 46.4, 67.7 and 81.6° are assigned to the (111), (200), (220) and (311) lattice planes of face centered cubic (fcc) crystalline Pt crystals (JCPDS No.01–1194) [44]. The chemical composition of Pt/e-RGO-SWCNT was further investigated by XPS analysis. The scan spectrum (Fig. 3c), indicates that the Pt/e-RGO-SWCNT catalyst is dominated by three elements belonged to the Pt 4f, C 1s, as well as O 1s signals. The HR-XPS spectra of Pt in Pt/e-RGO-SWCNT (Fig. 3d) reveal two strong peaks arising from Pt $4f_{7/2}$ and Pt $4f_{5/2}$. The Pt 4f spectra can be further resolved into two peaks, demonstrating the coexistence of Pt and PtO/Pt(OH)$_2$ [45,46]. The two distinct peaks at 71.4 and 74.8 eV are attributed to metallic Pt while the small peaks around 72.0 and 77.1 eV are assigned to the oxides of Pt species [47]. Based on the peak intensity, confirming that Pt in the Pt/e-RGO-SWCNT film are dominated by metallic state, which is favorable for MOR.
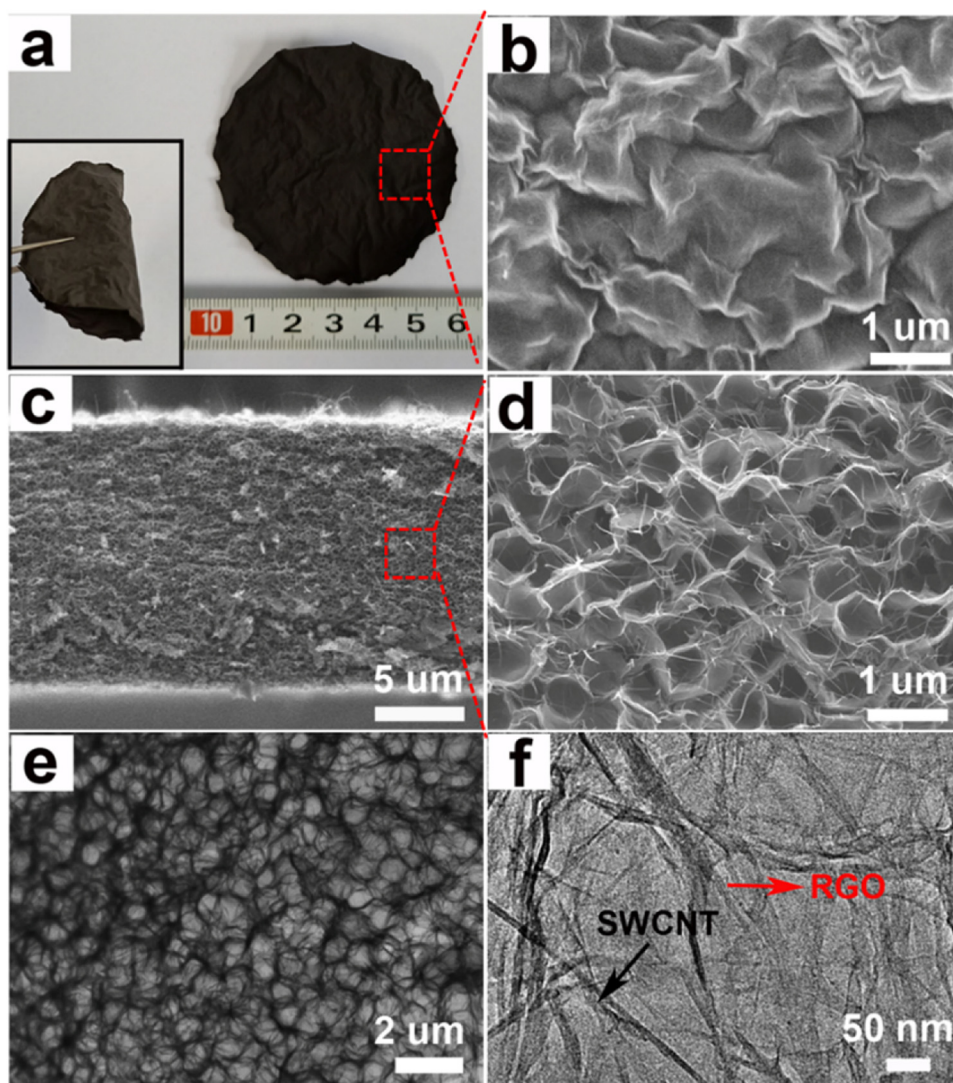
Fig. 1. (a) The digital photograph of a freestanding and flexible film of e-RGO-SWCNT (0.6) with the inset showing a folded film; (b) SEM image of the e-RGO-SWCNT (0.6); (c) Low-magnified SEM images of e-RGO-SWCNT in cross section; (d) High-magnified cross sectional SEM image of the red square in (c); (e, f) TEM and HRTEM images of e-RGO-SWCNT(0.6) film after calcination. (For interpretation of the references to colour in this figure legend, the reader is referred to the web version of this article).

3.2. Electrochemical characterization

Before electro catalytic measurement, CV and electrochemical impedance spectra (EIS) were performed in $[Fe(CN)_6]^{3-/4-}$ solutions to evaluate the electrochemical properties. The $K_3[Fe(CN)_6]/K_4[Fe(CN)_6]$ (1:1) mixture can be used as a redox probe to characterize the effective of electron transfer of the as-prepared electrodes [48,49]. The CV curves (see Fig. 4a) exhibit the $[Fe(CN)_6]^{3-/4-}$ reversible redox processes of Pt/RGO, Pt/e-RGO and Pt/e-RGO-SWCNT (0.6) electrodes. For Pt/e-RGO-SWCNT (0.6), the redox peak current is higher than those of

other samples, indicating its better electrochemical performance [5]. In addition, the Nyquist plots of EIS were carried out at 0.2 V to examine the internal resistances and interfacial charge-transfer behaviour of the products. As depicted in Fig. 4b, the diameter impedance arc (DIA) show the order as follows: Pt/RGO > Pt/e-RGO > Pt/e-RGO-SWCNT (0.6). This demonstrates the smallest charge transfer resistance and the best electrical conductivity, which is beneficial for the enhancements of electro catalytic performances [50].

Inspired by these good properties (electronic conductivity, large surface area, well-defined porous structure, and interconnected
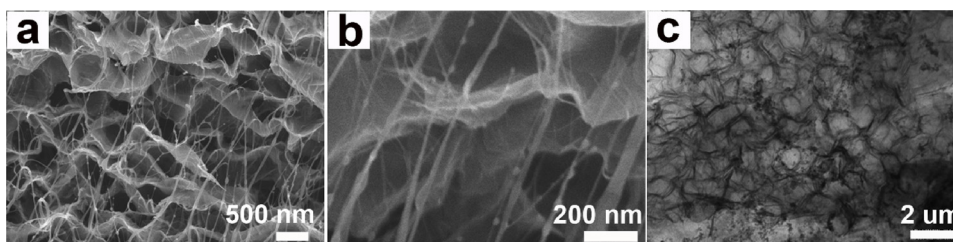
Fig. 2. (a, b) SEM images of the cross-section of Pt/e-RGO-SWCNT (0.6) at different magnification; (c) TEM image of Pt/e-RGO-SWCNT(0.6) film.
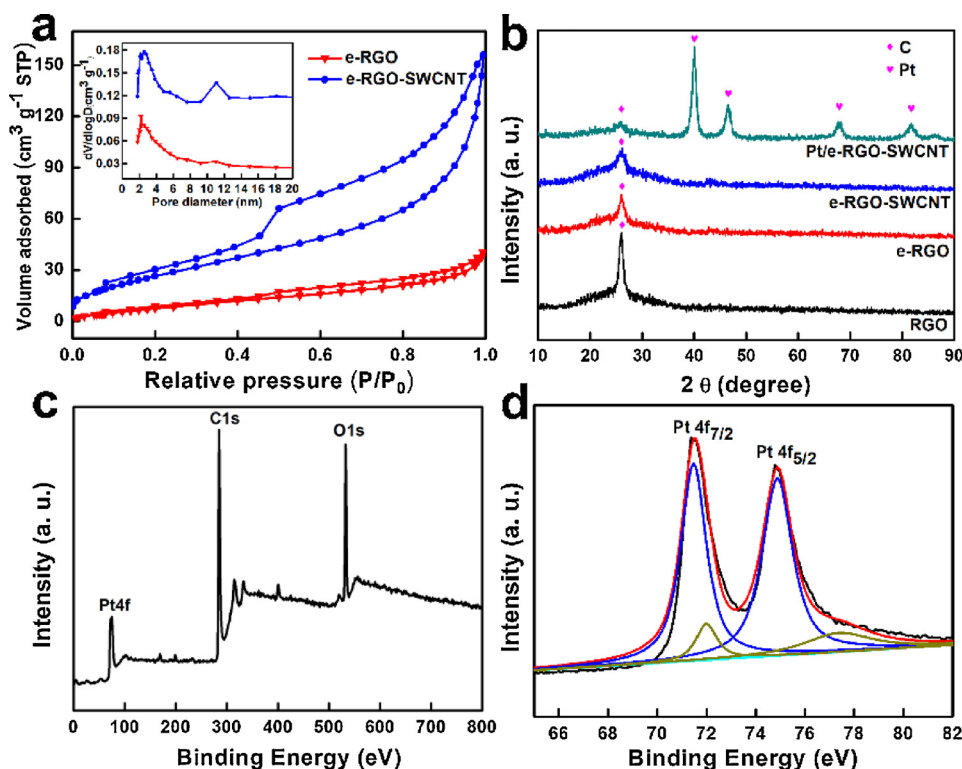
Fig. 3. (a) N_2 adsorption-desorption isotherms of e-RGO and e-RGO-SWCNT. The inset is the corresponding pore size distribution curves; (b) XRD patterns of RGO, e-RGO, e-RGO-SWCNT and Pt/e-RGO-SWCNT; XPS survey spectra of Pt/e-RGO-SWCNT paper (c) full scan, and its XPS spectrum corresponding to binding energies of (d) Pt 4f.

network), the Pt/e-RGO-SWCNT (0.6) are expected to exhibit outstanding electrochemical activity for MOR. To evaluate the superior electrochemical performance of the as-prepared sample, the electrochemically active surface areas (ECSAs) were firstly tested in 0.5 M H_2SO_4 at a scan rate of 50 mV s^{-1} (see Fig. 5a). The ECSAs can be calculated by hydrogen desorption processes according to the equation of ECSA = Q_H / 0.21 × m, where Q_H represents the charge for hydrogen adsorption/desorption (mC cm^{-2}), m is associated with the amount of Pt on the electrode, 0.21 (in mC cm^{-2}) is the monolayer charge (calculated from the surface density of 1.3×10^{15} atom cm^{-2}) [44]. As calculated, the ECSA value of Pt/e-RGO-SWCNT (0.6) is 13.31 m^2 g^{-1}, which is much higher than that of Pt/RGO (7.02 m^2 g^{-1}), Pt/e-RGO (9.71 m^2 g^{-1}) (see Fig. 5b). The elevated ECSA reveals the catalytic ability of the Pt/e-RGO-SWCNT (0.6) sample with more available active sites. The Pt/e-RGO-SWCNT is expected to show excellent electrocatalytic activities toward MOR. To make a comparison of the electrocatalytic performance of catalysts with different Pt loading, the membrane with four loadings of Pt of approximately 0.005 mg, 0.015 mg, 0.025 mg and 0.05 mg was first investigated in 0.5 M H_2SO_4 + 1.0 M CH_3OH at 50 mV s^{-1} (see Fig. S6). The current density of Pt/e-RGO-SWCNT (0.6) with 0.025 mg shows the highest

electrocatalytic activity among the other three catalysts. Therefore, a loading mass of Pt with 0.025 mg within all the-prepared catalyst for electrocatalysis was used.

The CV curves of as-prepared catalysts for MOR were performed in 0.5 M H_2SO_4 + 1.0 M CH_3OH solution, as shown in Fig. 5c. Two typical methanol oxidation peaks can be clearly observed: one peak loaded at the potential around 0.75 V in the forward scan is ascribed to the oxidation of methanol; while the other peak at about 0.5 V in the reverse scan is associated with the removal of the incomplete oxidized carbonaceous species during the forward scan. The corresponding mass and specific activities obtained from the current density normalized to the Pt mass loading and ECSA, respectively, are summarized in Fig. 5d and Table S1. The Pt/e-RGO-SWCNT (0.6) exhibits the highest mass and specific activities for MOR. As shown in Fig. 5d, the peak current density value of Pt/e-RGO-SWCNT (0.6) reaches to 1.45 mA cm^{-2}, which is greater than that of Pt/e-RGO (1.14 mA cm^{-2}) and Pt/RGO (1.00 mA cm^{-2}). Moreover, the peak current densities of Pt/e-RGO-SWCNT (0.6), Pt/e-RGO, and Pt/RGO are 191.7, 109.7 and 68.5 mA mg^{-1}, respectively. The mass activity of Pt/e-RGO-SWCNT (0.6) has a remarkable enhancement of 1.74 and 2.80 times higher than that of Pt/e-RGO and Pt/RGO, respectively. The higher electrochemical properties
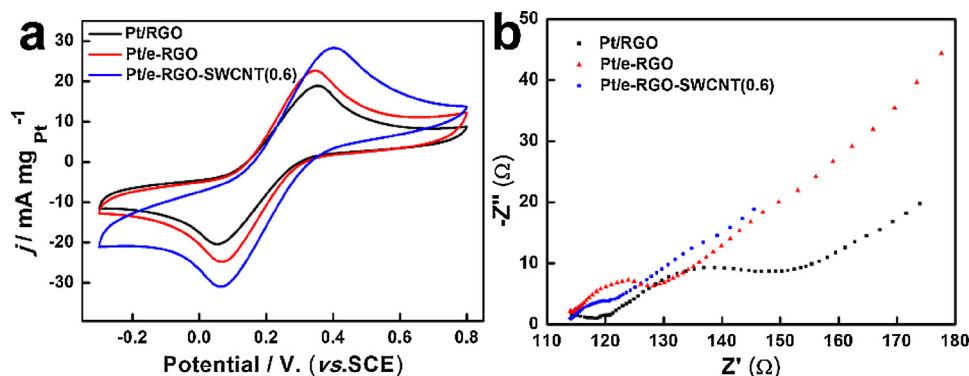

Fig. 4. (a) CVs and (b) Nyquist plots of electrode materials in a 5 mM [Fe(CN)6]$^{3-/4-}$ mixture (1:1) containing 0.1 M KCl solution at a potential of 0.2 V.
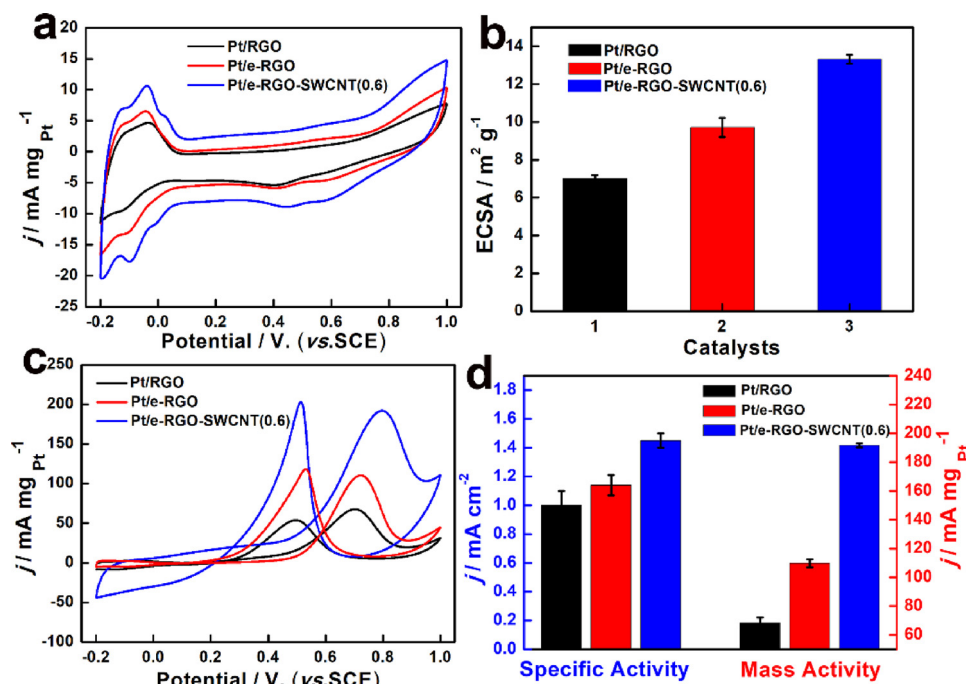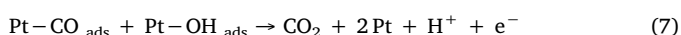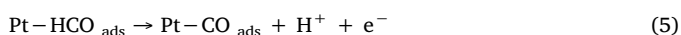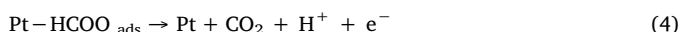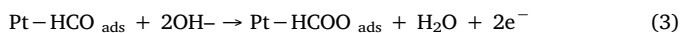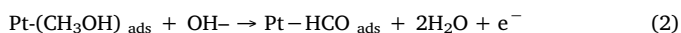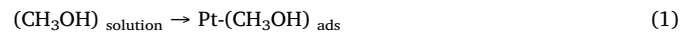
Fig. 5. CVs of the different electrodes recorded in (a) 0.5 M H_2SO_4 and (c) 0.5 M H_2SO_4 + 1 M CH_3OH. (b) The histograms of ECSAs of as-prepared samples. (d) Specific activity and mass activity of different electrocatalysts for methanol oxidation.

of Pt/e-RGO-SWCNT (0.6) can be ascribed to these major factors: (1) the porous of e-RGO and SWCNT can afford high ECSA and good electrical conductivity, resulting in remarkable electrochemical performance; and (2) the SWCNT act as the unique "superhighways" for rapid electron diffusions in the catalytic system. Meanwhile, the current density of Pt/e-RGO-SWCNT (0.6) catalyst is higher than that of JM Pt/C (Fig. S7) and many recent electrocatalysts, including carbon supported Pt-based catalysts, unsupported monometallic Pt electrocatalysts, and unsupported Pt based alloys or core-shell catalysts (Table S2). Recently, novel catalysts have been already prepared, however, the progress of catalyst in fuel cells is still at its early stage and the state-of-the-art hybrid electrodes cannot satisfy practical requirements of future fuel cells (*e.g.* low cost, and flexibility, *etc*.). In general, the Pt/e-RGO-SWCNT (0.6) catalyst exhibit the highest electrocatalytic activity specific activity, compared to various Pt-based catalysts towards methanol oxidation. More importantly, the as-prepared catalyst without binder was loaded on the 3D porous e-RGO-SWCNT skeleton with flexible and robust, which provides superior mass transfer and electrolyte mobility, high surface areas and suitable space for the electrocatalysis reaction. According to the established reaction mechanism for the electro-oxidation of methanol on Pt in alkaline medium, the methanol can be oxidized to CO_2. The mechanism of methanol electro-oxidation can be supposed as the following steps [51,52].

$$(CH_3OH)_{solution} \rightarrow Pt\text{-}(CH_3OH)_{ads} \tag{1}$$

$$Pt\text{-}(CH_3OH)_{ads} + OH^- \rightarrow Pt-HCO_{ads} + 2H_2O + e^- \tag{2}$$

$$Pt-HCO_{ads} + 2OH^- \rightarrow Pt-HCOO_{ads} + H_2O + 2e^- \tag{3}$$

$$Pt-HCOO_{ads} \rightarrow Pt + CO_2 + H^+ + e^- \tag{4}$$

$$Pt-HCO_{ads} \rightarrow Pt-CO_{ads} + H^+ + e^- \tag{5}$$

$$Pt + OH^- \rightarrow Pt-OH_{ads} + e^- \tag{6}$$

$$Pt-CO_{ads} + Pt-OH_{ads} \rightarrow CO_2 + 2Pt + H^+ + e^- \tag{7}$$

To investigate the stabilities of as-prepared three electrocatalysts, chronoamperometry measurements performed at 0.6 V in 0.5 M H_2SO_4 + 1 M CH_3OH solution for 4000 s are depicted in Fig. 6a. The

mass activities of all the samples decay rapidly at the initial stage and then reach to a stable value over time. In general, the loss of the catalytic activity may result from the Pt catalyst poisoning caused by chemisorption of intermediate products (such as CO-like species) [48,53,54] and some dissolution loss of the Pt [55]. During the whole measurement, Pt/e-RGO-SWCNT (0.6) retains the higher current density compared to Pt/e-RGO and Pt/RGO electrodes. After 4000 s, the mass activity is 7.78 mA mg^{-1} for Pt/e-RGO-SWCNT (0.6); 4.32 mA mg^{-1} for Pt/e-RGO; and 3.59 mA mg^{-1} for Pt/e-RGO. Additionally, the durability of the catalyst was further investigated by successive scans for 700 cycles (see Fig. 6b). Impressively, the current density on the Pt/e-RGO-SWCNT (0.6) is always higher than that on Pt/e-RGO and Pt/RGO over 700 cycles. After 700 cycles, the MOR mass activity on the Pt/e-RGO-SWCNT (0.6) film was found to be 27.1 mA mg^{-1}, *i.e.*, 2.2 and 4.3 times higher than on Pt/e-RGO (12.2 mA mg^{-1}) and Pt/RGO (6.2 mA mg^{-1}), respectively. All these results confirm that Pt/e RGO-SWCNT (0.6) film possesses the higher activity and durability, which makes it a promising catalyst for MOR. Moreover, the SEM of Pt/e RGO-SWCNT (0.6) was measured after reaction. As seen from Fig. S8, the morphology of the sample was largely maintained after CV scans, suggesting the stability of sample after reaction.

To explore the influence of pore diameter of PS on the MOR, the Pt nanoparticles were electrodeposited on e-RGO-SWCNT with different sizes of PS (200 nm, 600 nm and 3 μm). The electrocatalytic properties of Pt/e-RGO-SWCNT (0.2), Pt/e-RGO-SWCNT (0.6) and Pt/e-RGO-SWCNT (3) samples were evaluated by CV in 0.5 M H_2SO_4 within −0.2–1.0 V (see Fig. 7a). For Pt/e-RGO-SWCNT (0.6), the hydrogen adsorption and desorption peak located between −0.2 and 0.12 V is higher than Pt/e-RGO-SWCNT (0.2) and Pt/e-RGO-SWCNT (3). By measuring from the hydrogen adsorption-desorption area from CV cycles, as summarized in Fig. 7b and Table S1, the corresponding values of ECSA are calculated to be 9.45, 13.31 and 11.58 m^2 g^{-1} for Pt/e-RGO-SWCNT (0.2), Pt/e-RGO-SWCNT (0.6) and Pt/e-RGO-SWCNT (3), respectively. Similarly, Pt/e-RGO-SWCNT (0.6) with remarkable ECSA also reveals excellent electro catalytic performance for the MOR. Fig. 7c shows the CV curves of as-prepared samples carried out in 0.5 M H_2SO_4 + 1.0 M CH_3OH at 50 mV s^{-1}. The forward peak at
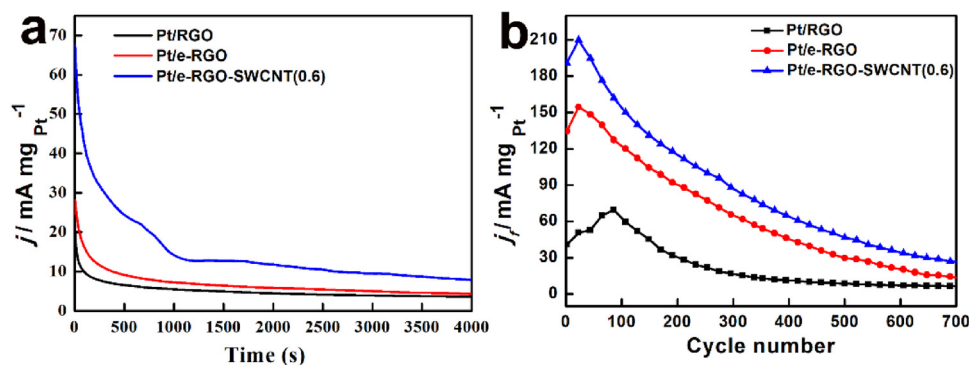
Fig. 6. (a) The chronoamperometric curves of Pt/RGO, Pt/e-RGO, Pt/e-RGO-SWCNT electrodes in methanolic acidic medium recorded at 0.6 V; (b) The peak current of methanol oxidation in the forward scan of as-prepared electrocatalysts *vs.* the CV cycle number.

approximately 0.8 V is associated with the oxidation of chemisorbed species coming from methanol adsorption, while the residual carbonaceous species are eliminated at the potential of 0.55 V in the backward scan [56]. Fig. 7d illustrates the mass and specific activities of as-prepared samples normalized to the surface area and Pt loading weight. Remarkably, the Pt/e-RGO-SWCNT (0.6) shows the maximum mass and specific activities among all the catalyst. The peak current density of Pt/e-RGO-SWCNT (0.6) is 191.7 mA mg_{Pt}^{-1}, which is 1.6 and 1.3 times greater than that of Pt/e-RGO-SWCNT (0.2) and Pt/e-RGO-SWCNT (3), respectively. Besides, the specific activity of Pt/e-RGO-SWCNT (0.6) is measured to be 1.45 mA cm^{-2} compared with Pt/e-RGO-SWCNT (0.2) (1.32 mA cm^{-2}) and Pt/e-RGO-SWCNT (3) (1.27 mA cm^{-2}) catalysts.

To exploit the practical application, the Pt/e-RGO-SWCNT (0.6) with different deformations, such as folded and rolled, was also used a flexible electrode for MOR. Fig. 8 shows the CV profiles of the composite films in the form of as-prepared, folded and rolled. The mass activities of folded and rolled Pt/e-RGO-SWCNT (0.6) catalysts are 171.4 and 160.8 mA mg^{-1}, respectively, which is slightly lower than the as-prepared films (191.7 mA mg^{-1}). The slightly reduced electrocatalytic activities of the deformed films are probably attributed to the slightly reduced ECSA and conductivity, which is not favor in mass

diffusion and the electronic transport [57]. Such good electrocatalytic ability of the film employing the folded and rolled states certifies the Pt/e-RGO-SWCNT (0.6) film as a flexible and bendable electrode for application potential in wearable devices.

4. Conclusion

In conclusion, we have developed a facile strategy for the synthesis of a freestanding Pt/e-RGO-SWCNT paper with flexible 3D porous architecture. During the process, the PS spheres as hard templates have been certified to be essential for preventing RGO sheets from aggregation, and the introduction of SWCNT as conductive skeletons loading electrolyte penetrate through e-RGO and thus wave them into a scalable film. The resultant freestanding porous Pt/e-RGO-SWCNT catalyst exhibits much better activity and durability towards MOR than those of Pt/e-RGO and Pt/RGO catalysts. Most importantly, under the various distorted states, such as folded and rolled states, the electrocatalytic performance of Pt/e-RGO-SWCNT is almost the same as the normal state, which makes Pt/e-RGO-SWCNT film a promising flexible catalysts for MOR. We envisioned that this work could offer general guidance for obtaining flexible and freestanding catalysts with high
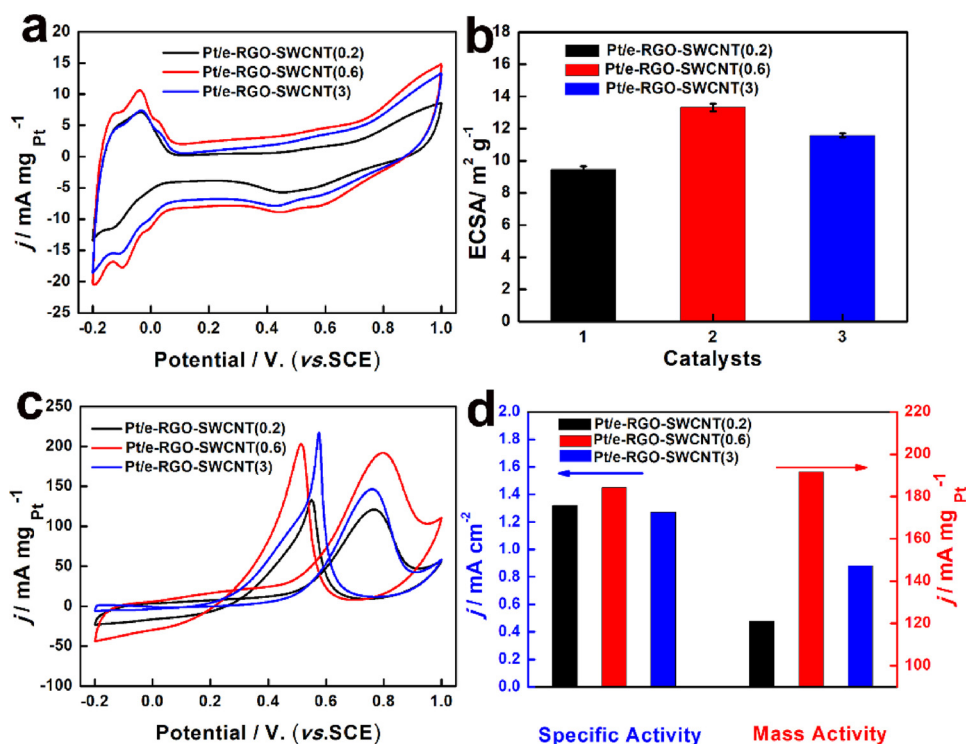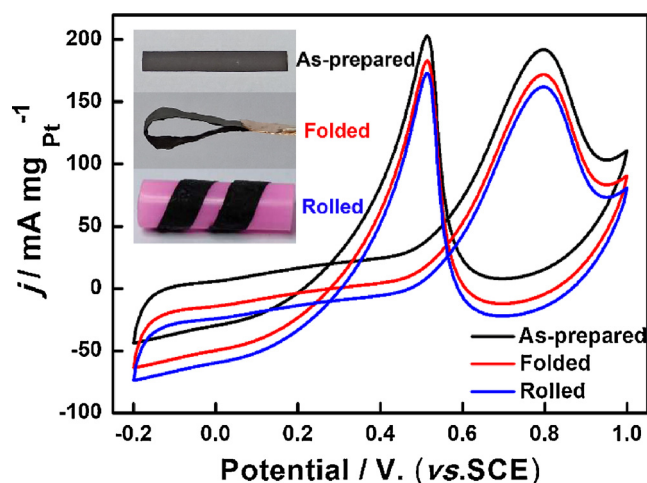

Fig. 7. Comparison of electrocatalytic activities of the Pt/e-RGO-SWCNT (0.2), Pt/e-RGO-SWCNT (0.6) and Pt/e-RGO-SWCNT (3) electrodes. CVs recorded in (a) 0.5 M H_2SO_4 solution and its (b) corresponding histogram of calculated ECSA values. (c) CV curves of the as-prepared catalysts toward MOR in 0.5 M H_2SO_4 + 1.0 M CH_3OH at 50 mV s^{-1}. (d) The catalytic performances of these three electrocatalysts.

Fig. 8. CVs of Pt/e-RGO-SWCNT catalyst toward MOR in 0.5 M H_2SO_4 + 1.0 M CH_3OH at 50 mV s^{-1} with different deformed states: as-prepared, folded, and rolled. Note that the rolled film was immobilized on insulating plastic substrates.

performances for fuel cells.

Acknowledgements

Appendix A. Supplementary data

Supplementary material related to this article can be found, in the online version, at doi:https://doi.org/10.1016/j.apcatb.2019.117886.

References

[1] L. Li, Z. Wu, S. Yuan, X.-B. Zhang, Energy Environ. Sci. 7 (2014) 2101–2122.
[2] N. Li, Z. Chen, W. Ren, F. Li, H.-M. Cheng, Proc. Natl. Acad. Sci. 109 (2012) 17360–17365.
[3] Z. Weng, Y. Su, D.W. Wang, F. Li, J. Du, H.M. Cheng, Adv. Energy Mater. 1 (2011) 917–922.
[4] K. Lu, J. Zhang, Y. Wang, J. Ma, B. Song, H. Ma, ACS Sustain. Chem. Eng. 5 (2016) 821–827.
[5] Q. Zhang, L. Jiang, H. Wang, J. Liu, J. Zhang, Y. Zheng, F. Li, C. Yao, S. Hou, ACS Sustain. Chem. Eng. 6 (2018) 7507–7514.
[6] Z.L. Wang, D. Xu, H.-X. Zhong, J. Wang, F.L. Meng, X.B. Zhang, Sci. Adv. 1 (2015) e1400035.
[7] F.L. Meng, Z.L. Wang, H.X. Zhong, J. Wang, J.M. Yan, X.B. Zhang, Adv. Mater. 28 (2016) 7948–7955.
[8] K.H. Liu, H.X. Zhong, S.J. Li, Y.X. Duan, M.M. Shi, X.B. Zhang, J.M. Yan, Q. Jiang, Prog. Mater. Sci. 92 (2018) 64–111.
[9] H.X. Zhong, Y. Zhang, X.B. Zhang, Chem 4 (2018) 196–198.
[10] Z.L. Wang, D. Xu, J.J. Xu, X.B. Zhang, Chem. Soc. Rev. 43 (2014) 7746–7786.
[11] H.X. Zhong, J. Wang, Y.W. Zhang, W.L. Xu, W. Xing, D. Xu, Y.F. Zhang, X.B. Zhang, Angew. Chem. Int. Ed. 53 (2014) 14235–14239.
[12] X. Jia, Z. Chen, A. Suwarnasarn, L. Rice, X. Wang, H. Sohn, Q. Zhang, B.M. Wu, F. Wei, Y. Lu, Energy Environ. Sci. 5 (2012) 6845–6849.
[13] K. Lu, D. Li, X. Gao, H. Dai, N. Wang, H. Ma, J. Mater. Chem. A Mater. Energy Sustain. 3 (2015) 16013–16019.
[14] M. Winter, R.J. Brodd, Chem. Rev. 104 (2004) 4245–4269.
[15] F. Yan, D. Guo, J. Kang, L. Liu, C. Zhu, P. Gao, X. Zhang, Y. Chen, Electrochim. Acta 283 (2018) 755–763.
[16] T. Ouyang, Y.Q. Ye, C.Y. Wu, K. Xiao, Z.Q. Liu, Angew. Chem. Int. Ed. 58 (2019) 4923–4928.
[17] X. Lu, C. Zhao, Nat. Commun. 6 (2015) 1–7.
[18] F. Meng, H. Zhong, D. Bao, J. Yan, X. Zhang, J. Am. Chem. Soc. 138 (2016) 10226–10231.
[19] W. Zeng, L. Shu, Q. Li, S. Chen, F. Wang, X.M. Tao, Adv. Mater. 26 (2014) 5310–5336.
[20] J. Huang, R.B. Kaner, Angew. Chem. 116 (2004) 5941–5945.
[21] W. Zeng, X.M. Tao, S. Chen, S. Shang, H.L.W. Chan, S.H. Choy, Energy Environ. Sci. 6 (2013) 2631–2638.
[22] T. Yamada, Y. Hayamizu, Y. Yamamoto, Y. Yomogida, A. Izadi-Najafabadi, D.N. Futaba, K. Hata, Nat. Nanotech. 6 (2011) 296–301.
[23] L.L.G.D. Arco, Y. Zhang, C.W. Schlenker, K. Ryu, M.E. Thompson, C. Zhou, ACS Nano 4 (2010) 2865–2873.
[24] J. Luo, J. Liu, Z. Zeng, C.F. Ng, L. Ma, H. Zhang, J. Lin, Z. Shen, H.J. Fan, Nano Lett. 13 (2013) 6136–6143.
[25] D. Wang, D. Hu, R. Kou, J. Zhang, D. Choi, G.L. Graff, Z. Yang, J. Liu, Z. Nie, Juan Li, M.A. Pope, I.A. Aksay, ACS Nano 4 (2010) 1587–1595.
[26] A.A. Balandin, S. Ghosh, W. Bao, I. Calizo, D. Teweldebrhan, F. Miao, C.N. Lau, Nano Lett. 8 (2008) 902–907.
[27] C. Lee, X. Wei, J.W. Kysar, J. Hone, Science 321 (2008) 385–388.
[28] D. Li, M.B. Muller, S. Gilje, R.B. Kaner, G.G. Wallace, Nature Nanotech. 3 (2008) 101–105.
[29] X. Yang, J. Zhu, L. Qiu, D. Li, Adv. Mater. 23 (2011) 2833–2838.
[30] S. Chen, J. Duan, J. Ran, M. Jaroniec, S.Z. Qiao, Energy Environ. Sci. 6 (2013) 3693–3699.
[31] M.F. El-Kady, V. Strong, S. Dubin, R.B. Kaner, Science 3 (35) (2012) 1326–1330.
[32] R. Zhang, X. Li, L. Zhang, S. Lin, H. Zhu, Adv. Sci. 3 (2016) 1600208–1600216.
[33] C. Tang, G. Long, X. Hu, K.W. Wong, W.M. Lau, M. Fan, J. Mei, T. Xu, B. Wang, D. Hui, Nanoscale 6 (2014) 7877–7888.
[34] C. Zhang, V.J. Pansare, R.K. Prud'homme, R.D. Priestley, Soft Matter 8 (2012) 86–93.
[35] L. Zhang, M. D'Acunzi, M. Kappl, Gn.K. Auernhammer, D. Vollmer, Langmuir 25 (2009) 2711–2717.
[36] Z. Yao, R. Yue, C. Zhai, F. Jiang, H. Wang, Y. Du, C. Wang, P. Yang, Int. J. Hydrogen Energy 38 (2013) 6368–6376.
[37] H. Sun, Z. Xu, C. Gao, Adv. Mater. 25 (2013) 2554–2560.
[38] C. Zhai, M. Zhu, D. Bin, H. Wang, Y. Du, C. Wang, P. Yang, ACS Appl. Mater. Interfaces 6 (2014) 17753–17761.
[39] C.W. Kuo, L.-M. Huang, T.C. Wen, A. Gopalan, J. Power Sources 160 (2006) 65–72.
[40] T. Chen, Z. Zhang, B. Cheng, R. Chen, Y. Hu, L. Ma, G. Zhu, J. Liu, Z. Jin, J. Am. Chem. Soc. 139 (2017) 12710–12715.
[41] Y. Sun, H. Zheng, C. Wang, M. Yang, A. Zhou, H. Duan, Nanoscale 8 (2016) 1523–1534.
[42] B. Zhao, J. Song, T. Fang, P. Liu, Z. Jiao, H. Zhang, Y. Jiang, Mater. Lett. 67 (2012) 24–27.
[43] Z. Qi, C. Xiao, C. Liu, T.W. Goh, L. Zhou, R. Maligal-Ganesh, Y. Pei, X. Li, L.A. Curtiss, W. Huang, J. Am. Chem. Soc. 139 (2017) 4762–4768.
[44] S. Wu, J. Liu, Z. Tian, Y. Cai, Y. Ye, Q. Yuan, C. Liang, ACS Appl. Mater. Interfaces 7 (2015) 22935–22940.
[45] I.A. Khan, Y. Qian, A. Badshah, D. Zhao, M.A. Nadeem, ACS Appl. Mater. Interfaces 8 (2016) 20793–20801.
[46] C. Zhai, J. Hu, M. Sun, M. Zhu, Appl. Surf. Sci. 430 (2018) 578–584.
[47] S. Fu, C. Zhu, D. Du, Y. Lin, ACS Appl. Mater. Interfaces 8 (2016) 6110–6116.
[48] M. Zhu, C. Zhai, M. Sun, Y. Hu, B. Yan, Y. Du, Appl. Catal. B: Environ. 203 (2017) 108–115.
[49] R. Yue, H. Wang, D. Bin, J. Xu, Y. Du, W. Lu, J. Guo, J. Mater. Chem. A Mater. Energy Sustain. 3 (2015) 1077–1088.
[50] H. Xu, B. Yan, K. Zhang, J. Wang, S. Li, C. Wang, Y. Shiraishi, Y. Du, P. Yang, Electrochim. Acta 245 (2017) 227–236.
[51] C. Zhai, M. Sun, L. Zeng, M. Xue, J. Pan, Y. Du, M. Zhu, Appl. Catal. B: Environ. 243 (2019) 283–293.
[52] Y.X. Chen, A. Miki, S. Ye, H. Sakai, M. Osawa, J. Am. Chem. Soc. 125 (2003) 3680–3681.
[53] M. Cao, D. Wu, R. Cao, ChemCatChem 6 (2014) 26–45.
[54] J. Hu, C. Zhai, C. Yu, L. Zeng, Z.Q. Liu, M. Zhu, J. Colloid Interface Sci. 524 (2018) 195–203.
[55] D. Bin, B. Yang, F. Ren, K. Zhang, P. Yang, Y. Du, J. Mater. Chem. A Mater. Energy Sustain. 3 (2015) 14001–14006.
[56] Y. Kang, J.B. Pyo, X. Ye, T.R. Gordon, C.B. Murray, ACS Nano 6 (2012) 5642–5647.
[57] J. Wang, P. Zhang, Y. Xiahou, D. Wang, H. Xia, H. Mohwald, ACS Appl. Mater. Interfaces 10 (2018) 602–613.